

# Voltage-Dependent Activation Energy Maps for Analytic Lifetime Modeling of NBTI Without Time Extrapolation

Katja Puschkarsky<sup>1</sup>, Member, IEEE, Hans Reisinger, Christian Schlünder, Wolfgang Gustin, and Tibor Grasser, Fellow, IEEE

**Abstract**—To enable MOSFETs lifetime extrapolation of up to 10 years, bias temperature instability (BTI) is commonly accelerated via increased stress voltage and increased temperature. We demonstrate that BTI can be described by a unique activation energy map including the voltage and temperature dependence of stress and recovery and use capture and emission time maps to model the time dynamics responsible for the threshold voltage shift of BTI. Based on this approach, we present a new measurement technique, further called temperature-accelerated measure-stress-measurements (TA-MSM) enabling lifetime modeling of BTI without any time extrapolation. We show the application of this technique to simulate standard qualification measurements, fast wafer-level reliability measurements as well as the degradation after ac and dc burn-in stress. In addition, we show that the TA-MSM technique is a valuable tool for the study of the permanent component and the recently discovered reverse recovery effect.

**Index Terms**—Activation energy maps, bias temperature instability (BTI), modeling.

## I. INTRODUCTION

THERE have been numerous publications identifying the negative bias temperature instability (NBTI) as one of the most critical reliability issues for silicon-based MOSFETs [1]–[3]. In a good approximation, NBTI can be understood as the collective response of many independent defects [4], [5]. The kinetics of these defects can be described by capture and emission time (CET) constants for each individual defect [6], where the time constants correspond to the

reciprocal rates of chemical reactions [7]. The CET constants are widely distributed, and the investigation of the physical mechanisms of BTI requires stress and recovery times of several decades in time (further called experimental window [9], [10]). The experimental window is limited by the measurement time available and the measurement delay introduced by the measurement equipment ( $t_d \approx 1 \mu\text{s}$  [11]). The temperature dependence of individual defect time constants for capture and emission follows the Arrhenius law [13]:

$$\tau = \tau_0 \cdot \exp\left(\frac{E_a}{k_B T}\right) \quad (1)$$

with an activation energy  $E_a$ , Boltzmann's constant  $k_B$ , and the characteristic temperature-independent constant  $\tau_0$ . For recovery and degradation, it has been shown independently by Pobegen and Grasser [14] that this temperature dependence of the CET constants is also valid for a large ensemble of defects. Following (1), we can calculate the change in defect time constant  $\tau_1$  to  $\tau_2$  when changing the temperature from  $T_1$  to  $T_2$

$$\tau_2 = \tau_0 \left(\frac{\tau_1}{\tau_0}\right)^{\frac{T_1}{T_2}}; \quad \frac{\log(\tau_1/\tau_0)}{\log(\tau_2/\tau_0)} = \frac{T_2}{T_1}. \quad (2)$$

After the determination of  $\tau_0$ , the data recorded at a temperature  $T_1$  can be drawn as a function of the time equivalent to a temperature, referred to as temperature time  $\Theta(T_2)$  [15].

In Fig. 1(a), schematic for the temperature acceleration of defects within the experimental window is illustrated. To enlarge the equivalent measurement window, simply increasing the temperature would accelerate both degradation and recovery, the experimental window in Fig. 1 would shift right/up. Thus, information about defects with short CET constants [e.g., shorter than 0.1 ms at  $T = 100^\circ\text{C}$  (see red-dashed area) with  $\tau_0 = 10^{-14}$  s] would be lost and would move out of the experimental window. The measurement technique introduced in Section II overcomes this drawback and achieves measurement of the CET constants of  $1 \mu\text{s}$  while covering equivalent stress and recovery times of more than 10 years. The concept of activation energy maps is explained in Section III. In Section IV, in contrast to Pobegen *et al.* [15], we demonstrate for degradation and recovery simultaneously that also for devices with a large number of defects and widely distributed time constants, the temperature activation of capture and emission follows the Arrhenius law. We further

Manuscript received June 28, 2018; revised August 28, 2018; accepted September 8, 2018. Date of publication October 5, 2018; date of current version October 22, 2018. This work has received funding from the BMBF and European Community's FP7 n°619234 (MoRV) as well as from the European Community Union through CATRENE project CT217 (RESIST). The review of this paper was arranged by Editor K. Kalna. (Corresponding author: Katja Puschkarsky.)

K. Puschkarsky is with the Institute for Microelectronics, Technische Universität Wien, 1040 Vienna, Austria, and also with Infineon Technologies AG, 85579 Neubiberg, Germany (e-mail: katja.puschkarsky@infineon.com).

H. Reisinger, C. Schlünder, and W. Gustin are with Infineon Technologies AG, 85579 Neubiberg, Germany (e-mail: hans.reisinger@infineon.com; christian.schlunder@infineon.com; wolfgang.gustin@infineon.com).

T. Grasser is with the Institute for Microelectronics, Technische Universität Wien, 1040 Vienna, Austria (e-mail: grasser@iue.tuwien.ac.at).

Color versions of one or more of the figures in this paper are available online at <http://ieeexplore.ieee.org>.

Digital Object Identifier 10.1109/TED.2018.2870170

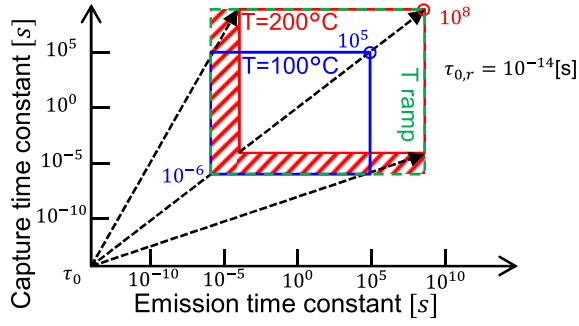


Fig. 1. Arrhenius temperature activation: the experimental window at  $T = 100^\circ\text{C}$  with stress and recovery times up to 100 ks (blue). Performing the same experiment at  $T = 200^\circ\text{C}$  shifts the CET constants into the measurement window at  $T = 100^\circ\text{C}$  of more than 10 years. With a limiting measurement delay of  $1\ \mu\text{s}$ , the shortest measurable equivalent CET constant at  $T = 200^\circ\text{C}$  is 0.1 ms (red lines). The new measurement technique (green-dashed lines) overcomes this drawback and covers CET constants of  $1\ \mu\text{s}$  to more than 10 years.

present voltage-dependent activation energy maps including  $V_{\text{stress}} \leq V_{\text{use}}$  enabling lifetime modeling of BTI without the need of time extrapolation. In Section V, we compare fast wafer-level reliability (fWLR) and burn-in stress measurements with the derived analytic model and we will show the usability of this technique to study the permanent component of BTI.

## II. EXPERIMENTAL DETAILS

Samples used were productive smart power pMOSFETs ( $W = 10\ \mu\text{m}$  and  $L = 130\ \text{nm}$ ) from a 130-nm technology, with a 2.2-nm nitrided gate oxide. The electrical measurements were performed with the ultrafast measure-stress-measure technique as described in [11]. To achieve an acceleration of the recovery and the ability to measure the capture and emission of defects with short emission times, a small electric oven has been constructed to perform temperature ramps. A major part of the accelerated recovery actually occurs during the temperature up-ramps after stress (see Fig. 3). Since  $V_{\text{th}}$  itself is a function of the temperature and decreases during the up-ramps, a first, prestress temperature ramp reference trace is needed to calculate the difference between a recovery trace after stress and the reference. The reproducibility of the temperature during the up-ramps is  $\pm 0.1\ \text{K}$ . With  $V_{\text{th}}(T) = 0.96 \pm 0.05\ \text{mV/K}$ , the accuracy of the  $\Delta V_{\text{th}}$  due to temperature changes is a factor of 10 below the measurement resolution of  $0.1\ \text{mV}$ . The temperature-accelerated (TA) measurement scheme illustrated in Fig. 2 with three different patterns has been developed to extend the experimental time window of degradation and recovery of  $1\ \mu\text{s}$  to more than 10 years with the application of temperature ramps as presented in [12] as follows.

- 1) For short stress times (below 1 ms), both the stress and the recovery temperature remain constant (e.g., at  $T = 100^\circ\text{C}$ , further called reference temperature).
- 2) For medium stress times (below 10 ks),  $T_{\text{rec}} = T_{\text{stress}}$ , after 1000 s  $T_{\text{rec}}$  is linearly increased by 100 K within 1000 s. Right before the next stress-recovery sequence, the sample is cooled down (not drawn) to the reference temperature.

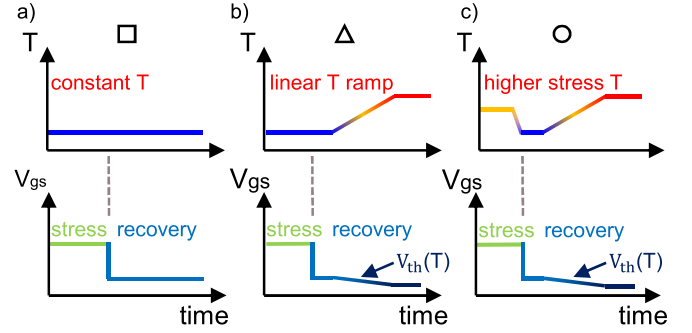


Fig. 2. TA-MSM measurement scheme. (a) Short stress times: constant  $T_{\text{stress}} = T_{\text{rec}}$ . (b) Medium stress times: for the first 1000 s, the  $T_{\text{rec}}$  is kept constant and is subsequently linearly increased by 100 K within 1000 s.  $V_{\text{th}}$  is a function of temperature and decreases during the temperature ramp. Right before the next stress sequence, the sample is cooled down. (c) Long stress times: increased  $T_{\text{stress}}$ . After stress, the temperature is decreased to  $T_{\text{rec}}$  while keeping the stress voltage applied. The measurement scheme for the recovery is the same as for medium stress times. The squares, triangles, and circles are indicated in Figs. 3, 4, and 12, which measurement sequence has been applied. During the up-ramps, the  $V_{\text{th}}$  itself decreases with the temperature.

- 3) To reduce the total stress time,  $T_{\text{stress}}$  is also increased. After stress, the temperature is decreased to the reference temperature while keeping the stress voltage applied to prevent recovery during cool-down. As soon as the reference temperature is reached, the same recovery temperature pattern is applied as after medium stress times.

## III. ACTIVATION ENERGY MAP

As demonstrated in [16], a wide range of experimentally observed features of NBTI can be explained in an analytical form using CET maps. The CET map model is based on a defect-centric model [7], [8] and assumes that the thermally activated charge exchange of independent defects lead to BTI. Charge exchange as well as first-order reactions creating interface states can be described in agreement with previous work by two bivariate Gaussian distributions [6], [17]: one bivariate Gaussian distribution for the oxide defects being mainly responsible for the recoverable component and one distribution for the interface defects which are mostly permanent in typical experimental windows [10], [18]. Main parameters of the analytic model are the mean values of the capture and emission activation energies  $E_{ac}$  and  $E_{ae}$  ( $\mu_c$  and  $\mu_e$ ) with their standard deviations ( $\sigma_c$  and  $\sigma_e$ ). In addition, we observe an increase of the emission activation energies  $E_{ae}$  with larger capture activation energies  $E_{ac}$ :  $E_{ae} = E_{ac} + \Delta E_{ae}$ . The correlation of the standard deviations is modeled as shown in [17]  $\sigma_e^2 = r\sigma_c^2 + \sigma_{\Delta_e}^2$ , with a correlation  $r = 1$  for the recoverable and no correlation  $r = 0$  for the permanent component. Thus, the charged trap density  $g(E_c, E_e)$  for each component is given as

$$g(E_c, E_e) = \frac{A}{2\pi\sigma_c\sigma_{\Delta_e}} \cdot \exp\left(-\frac{(E_c - \mu_c)^2}{2\sigma_c^2} - \frac{(E_e - (rE_c + \mu_{\Delta_e}))^2}{2\sigma_{\Delta_e}^2}\right) \quad (3)$$

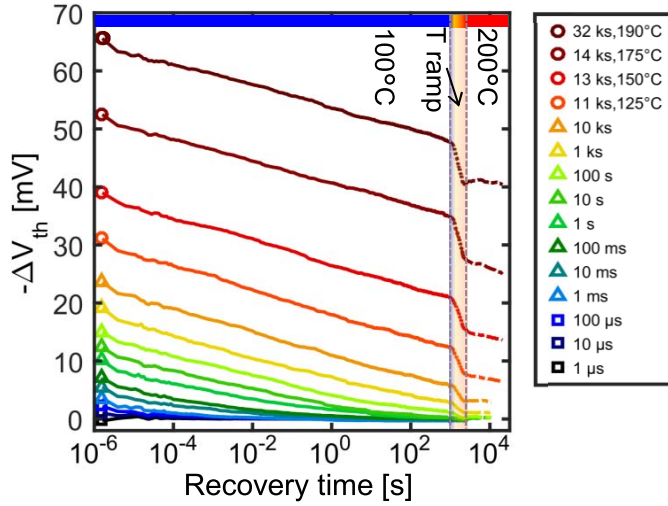


**Fig. 3.** Real-time measurement data of TA-MSM measurement with  $V_{gs} = -2$  V and  $T_{ref} = 100$  °C. The  $\Delta V_{th}$  is obtained subtracting the reference (including the temperature ramp) from the measurement data. The squares, triangles, and circles correspond to the measurement schemes shown in Fig. 2(a)–(c), respectively. Measurements with stress times longer than 1 ms start with 1000 s recovery at  $T=100$  °C, followed by a linear temperature ramp within 1000 s from 100 to 200 °C and further recovery at 200 °C. For the stress times up to 10 ks, the stress temperature is  $T = 100$  °C. The stress temperature is increased for stress times larger than 10 ks up to  $T = 190$  °C.

with the amplitudes  $A_r$ ,  $A_p$  (the amplitudes give the maximum obtainable degradation if all defects are charged). The threshold voltage shift after a stress time  $t_s$  and a recovery time  $t_r$  is the integral over all defects being charged up to the stress time  $t_s$  ( $\tau_c < t_s$ ) and not yet being discharged at the recovery time  $t_r$  ( $\tau_e > t_r$ ) [16]

$$\Delta V_{th}(t_s, t_r) = \int_{E_c=0}^{\infty} \int_{E_e=0}^{\infty} P(t_s, t_r) \times g(E_c, E_e) dE_c dE_e \quad (4)$$

with the  $P(t_s, t_r)$  defect occupancy map for each stress/recovery time (see [19]). The activation energy map is a temperature-independent map, while the CET maps at constant temperature are calculated using 1 with one characteristic temperature-independent constant  $\tau_{0,r}$  for the recoverable and  $\tau_{0,p}$  for the permanent defects [14].

#### IV. ACCELERATED NBTI MEASUREMENTS

To calibrate BTI lifetime models, several measurements at different temperatures are required. This is time consuming and requires a large number of test devices. Therefore, we perform TA measure-stress-measurements (TA-MSM) at constant stress voltage with linear temperature ramps as described in Section II. The TA-MSM results for a stress voltage of  $V_{gs} = -2$  V are shown in Fig. 3 on a logarithmic time scale. The reference temperature  $T_{ref} = 100$  °C is chosen to be higher than the typical temperature for industrial applications of  $T = 85$  °C. Each measurement after stress starts with 1000 s recovery at  $T = 100$  °C, followed by a linear temperature ramp of 1000 s from 100 to 200 °C and further recovery up to 20 ks at  $T = 200$  °C. The stress temperature is increased for stress times larger than 10 ks up to  $T = 190$  °C (see Fig. 2). Within the temperature ramp, an acceleration of the recovery

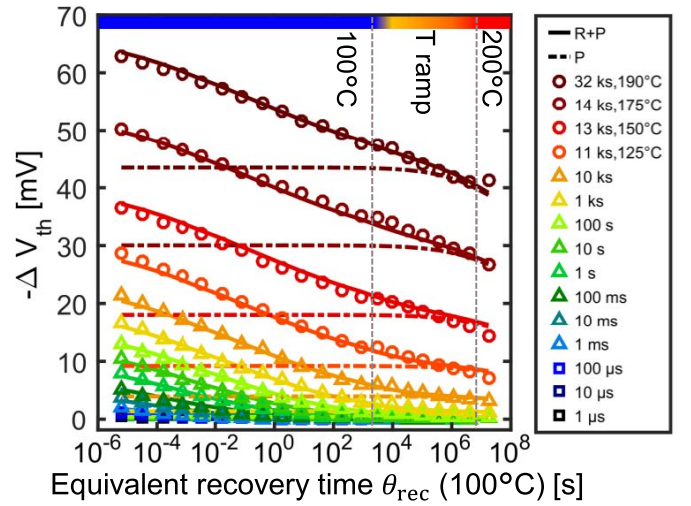


**Fig. 4.** Same measurement data (squares, triangles, and circles) as shown in Fig. 3, but with the calculated equivalent recovery times at  $T_1 = 100$  °C using the Arrhenius law [see (2)] with  $\tau_0 = \tau_{0,p} = 0.57$  ns, and  $T_2 = T_{meas}$  for every change in temperature. The squares, triangles, and circles correspond to the measurement scheme shown in Fig. 2(a)–(c), respectively. The gray vertical dashed lines mark the area of the temperature ramp. The analytic model fit for the recoverable and permanent component, obtained from the activation energy map, is shown as solid lines, the dashed lines correspond to the contribution of only the permanent component.

**TABLE I**  
ACTIVATION ENERGY MAP PARAMETERS OF FIG. 5

	$\tau_0$ (ns)	$\mu_c$ (eV)	$\sigma_c$ (eV)	$\mu_{\Delta e}$ (eV)	$\sigma_{\Delta e}$ (eV)	$A$ [V]
R	$5.5 \cdot 10^{-5}$	0.97	0.3	-0.08	0.2	0.07
P	0.57	1.28	0.1	1.47	0.2	0.14

of about four decades in time is visible (highlighted area in Fig. 3). We perform an automatized least-square minimization to the measurement data of Fig. 3 with the analytic activation energy map model (4). A summary of the fit parameters is given in Table I with  $\tau_{0,r} = 55$  fs for the recoverable component and  $\tau_{0,p} = 0.57$  ns for the more permanent component. Therefore, we can show in Fig. 4 the same data set as in Fig. 3, but with the equivalent recovery time  $\Theta(100$  °C) [see (2)] with  $\tau_0 = \tau_{0,p}$ . The acceleration of the recovery during the temperature ramp shown in Fig. 3 is stretched in time due to the time-temperature transformation with the Arrhenius law. The comparison of the measurement results (symbols) and the analytic model (lines) shows a very good agreement in the extremely wide time window of up to 10 years equivalent time  $\Theta(100$  °C). The applicability of this measurement acceleration has been shown by Puschkarsky *et al.* [12] with a very high agreement of the calibrated model with MSM measurements at constant temperatures.

The defect density as a function of the activation energy for charge capture and emission obtained is shown in Fig. 5(a) with the parameters (see Table I) solely obtained from the measurement data shown in Fig. 3. The square indicates the measurement range in the energy space of the TA-MSM measurements of Fig. 3. A recovery time of 100 ks at  $T = 200$  °C corresponds to an activation energy of 1.65 eV or more than  $10^8$  s at  $T = 100$  °C. The distribution of the permanent



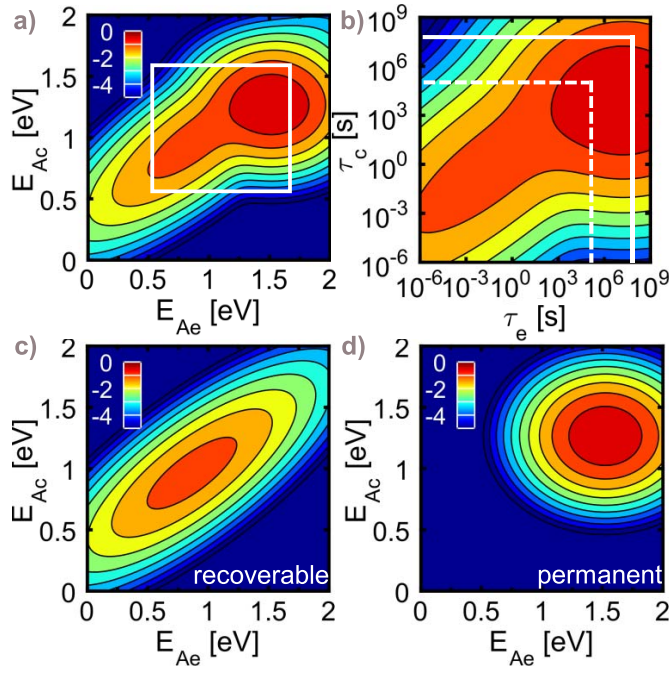


**Fig. 5.** Activation energy and CET maps extracted from the data of Fig. 3 for  $V_{gs} = -2$  V. All maps are shown on a logarithmic color scale, 0 corresponds to a  $\pm V_{th}$  of  $10^0$  mV/ $10^{-4}$  eV<sup>2</sup>. (a) Activation energy map for the recoverable and permanent component. White square: experimental window of Fig. 3. (b) CET map at  $T = 100$  °C calculated from (a) with the typical experimental window for constant temperature measurements (dashed square) and the experimental window achievable with the acceleration (solid square). (c) Activation energy map of the recoverable component. (d) Distribution of the activation energies of the permanent component.

component, shown in Fig. 5(d), is located at high capture activation energies and high emission activation energies, whereas the recoverable defects, shown in Fig. 5(c), have smaller and correlated capture activation and emission activation energies. In Fig. 5(b), the CET map at  $T = 100$  °C is shown, using  $\tau_{0,p}$  for the calculation of the CETs. The dashed lines indicate the measurement window for constant temperature measurements at  $T = 100$  °C. With this accelerated measurement technique, only one measurement has to be performed per stress/recovery voltage. As shown in Fig. 4, most of the recovery acceleration occurs during the temperature ramp, therefore, the additional recovery time after the highest temperature has been reached can be further reduced. The required measurement time for the accelerated activation energy map can, therefore, be reduced to less than 10 h, whereas traditional constant temperature measurements with the same measurement window would require at least 100 h of measurement time and minimum three different stress temperatures.

#### A. Voltage Dependence of the Activation Energy Map

Due to the reduced time effort, we are able to perform accelerated measurements at five different stress voltages ( $V_{gs, stress} = [-1, -1.5, -1.8, -2, -2.2]$  V, measurement scheme is as same as in Fig. 3) to obtain the stress voltage dependence of the activation energy maps. For each stress condition, a new sample is used. As shown exemplary in Fig. 6 for  $t_r = 1$   $\mu$ s,  $\Delta V_{th}$  increases exponentially with

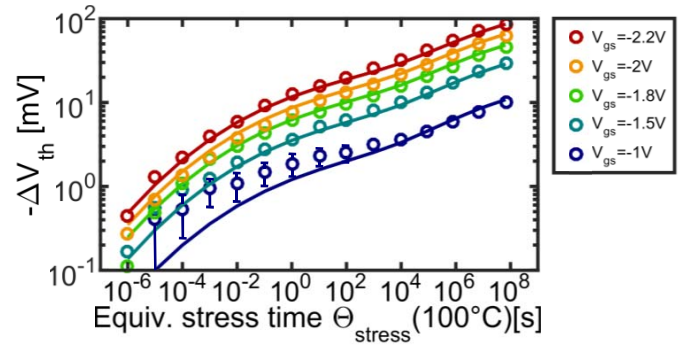


**Fig. 6.** Voltage-dependent TA-MSM: Threshold voltage shift with equivalent stress time (see temperatures in legend of Fig. 4) for different stress voltages shown with a recovery time of 1  $\mu$ s (at  $T = 100$  °C). The analytic model fit with the same voltage dependent activation energy map for all stress voltages is shown as solid lines.

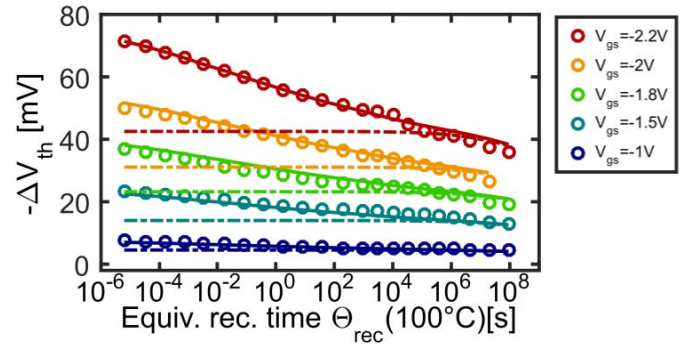


**Fig. 7.** Voltage-dependent TA-MSM: Threshold voltage shift with equivalent recovery time after  $t_{stress, equiv} = 10^8$  s for different stress voltages. The analytic model fit (permanent and recoverable components) with the same voltage-dependent activation energy map for all stress voltages, is shown as solid lines; the dashed lines correspond to the contribution of only the permanent component.

stress voltage and the dependence on the stress time remains roughly constant. In addition, the dependence of  $\Delta V_{th}$  on the recovery time (see Fig. 7) for all five stress voltages already indicates that the distribution of the CET constants does not change significantly with the stress voltage, while the number of active traps increases. To model this voltage dependence, we extended the model for the activation energy maps: The amplitudes of each component ( $A_r$  and  $A_p$ ) are modeled as  $A = (V_{stress}/V_0)^m$  with the constants  $m$  and  $V_0$  [16]. Furthermore, previous studies on individual defects on Si [13] have shown that the mean value  $\mu_c$  of each distribution is expected to linearly decrease with increasing stress voltage (capture times decrease with increasing stress voltage). We thus model the linear decrease with increasing stress voltage of  $\mu_c$  by  $\mu_c = \mu_{(c,0)} + k V_{stress}$ , where  $\mu_{(c,0)}$  denotes the mean value of the activation energy constants for the charge capture at 0 V and  $k$  is the voltage acceleration constant. We observe that the emission times remain unaffected by the stress voltage, accordingly, we model:  $\mu_{\Delta e} = \mu_{\Delta(e,0)} - k V_{stress}$ . The fits with the voltage-dependent activation energy map (lines in Figs. 6–8) show a very good agreement with the measurement data (circles). The obtained parameters for the amplitude are  $V_{(0,r)} = -4.77$ ,  $V_{(0,p)} = -4$ , and  $m_r = 3$ ,  $m_p = 2.8$ . The voltage dependence of the mean values ( $k_r = 0.01$  eV/V and

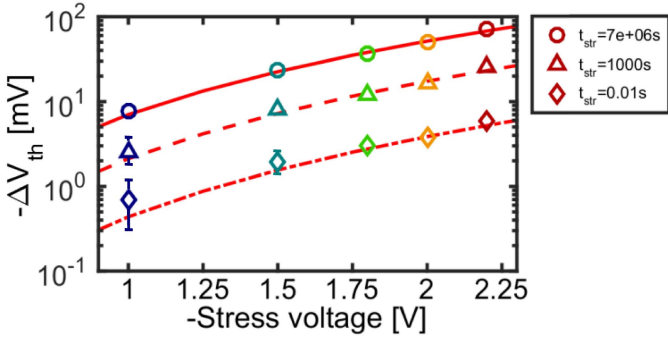


Fig. 8. Voltage-dependent TA-MSM: Threshold voltage shift with stress voltage after different stress times and  $t_{\text{rec}} = 1 \mu\text{s}$ . The analytic model fit (permanent and recoverable component) for each stress time with the same voltage-dependent activation energy map for all stress voltages is shown as solid/dashed/dotted line, respectively.

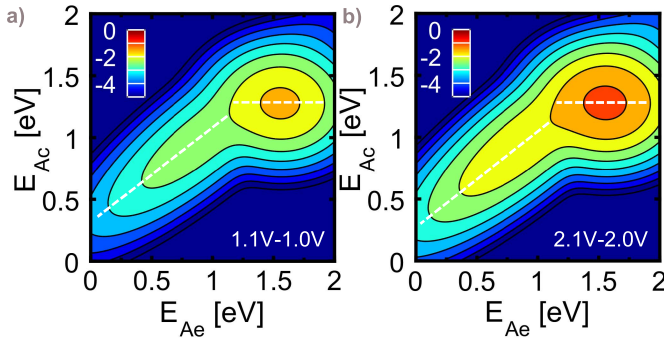


Fig. 9. Differential activation energy map obtained with the measurements shown in Fig. 6, showing the contribution of defects being activated within a change of stress from  $V_{\text{gs}} = V_1$  to  $V_{\text{gs}} = V_2$ . All maps are shown on a logarithmic color scale, 0 corresponds to a  $1 V_{\text{th}}$  of  $10^0 \text{ mV}/10^{-4} \text{ eV}^2$ . (a)  $V_2 = -1.1 \text{ V}$ ,  $V_1 = -1 \text{ V}$  and (b)  $V_2 = -2.1 \text{ V}$ ,  $V_1 = -2 \text{ V}$ .

$k_p = 0 \text{ eV/V}$ ) is weak compared to the bias dependence of the individual traps [16]. The reason for this is that with different gate bias also the energetically available traps in the oxide change [18].

To calculate the threshold voltage shift after arbitrary stress signals differential activation energy maps can be used. The differential activation energy map shows the defect additionally contributing to the threshold voltage shift when changing the stress voltage from  $V_1$  to  $V_2$ ,  $g(E_c, E_e)_{\text{diff}} = g(V_2) - g(V_1)$ . In Fig. 9(a) and (b), differential activation energy maps are shown for  $V_1 = 1 \text{ V}$ ,  $V_2 = 1.1 \text{ V}$ , and  $V_1 = 2 \text{ V}$ ,  $V_2 = 2.1 \text{ V}$ . Comparing Fig. 9(a) and (b), we observe a stronger voltage dependence of the amplitude for the more permanent component than for the recoverable component. Increasing the stress voltage, we observe a change in the capture of activation energies for the recoverable component, whereas no shift for the permanent component is observable (dashed lines as a guide to the eyes).

## V. APPLICATION

The measurement technique and the obtained activation energy maps presented here have a wide application spectrum. We present two applications, one for the comparison of fWLR data with standard qualification measurements and one for the modeling of burn-in stress. The standard lifetime models

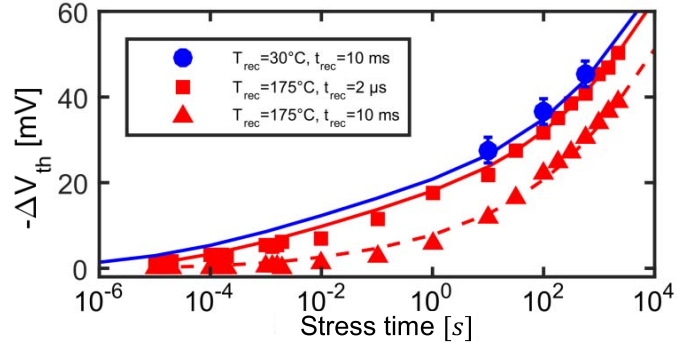
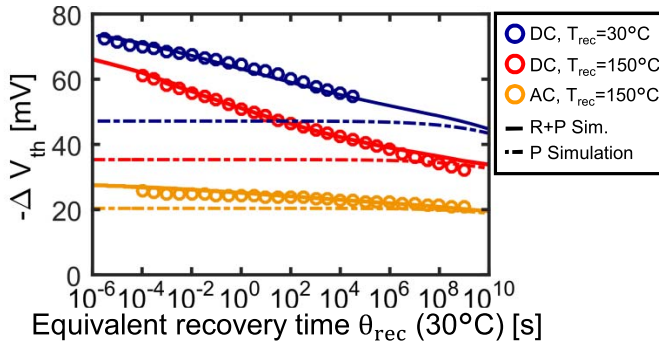


Fig. 10. Comparison of three different measurement techniques after the same NBTI stress at  $T = 175^\circ\text{C}$ ,  $V_{\text{gs}} = -2.2 \text{ V}$ . (a) fWLR measurement with the resistive heater  $T_{\text{rec}} = 30^\circ\text{C}$  with  $t_d = 10 \text{ ms}$ . (b) qualification measurement at  $T_{\text{rec}} = 175^\circ\text{C}$  with  $t_d = 10 \text{ ms}$  and measurements with the fast measurement technique at  $T_{\text{rec}} = 175^\circ\text{C}$  and  $t_d = 2 \mu\text{s}$ . Solid lines: simulated results obtained from the activation energy map.

obtained from qualification measurements cannot be used to calculate the fWLR drift limits due to the lack of calibrated models considering different measurement times and stress/recovery temperatures of qualification and fWLR measurements. Since fWLR measurements need to be quickly performed, stress times are limited to less than 1000 s. To obtain a measurable degradation, the temperature acceleration is often higher than during the standard qualification measurements. For fWLR measurements, standard measurement equipment with a measurement delay of  $t_d \approx 10 \text{ ms}$  is used, therefore it is crucial to reduce the amount of recovery within the measurement delay. A commonly applied technique is the use of resistive heaters [20] to perform the stress at high temperatures and measure the recovery at low temperatures. The stress voltage is kept applied until the heater is switched OFF, and the sample is cooled down to chuck temperature within seconds [21]. In Fig. 10, we compare three different measurement techniques with different equipment and  $V_{\text{gs}} = -2.2 \text{ V}$  and  $T_{\text{stress}} = 175^\circ\text{C}$ : 1) fWLR measurement with the resistive heater ( $T_{\text{rec}} = 30^\circ\text{C}$  and  $t_d = 10 \text{ ms}$ , blue circles); 2) standard qualification measurement ( $t_d = 10 \text{ ms}$  and  $T_{\text{rec}} = 175^\circ\text{C}$ , red triangles); and 3) the ultrafast measurement equipment ( $t_d = 2 \mu\text{s}$  and  $T_{\text{rec}} = 175^\circ\text{C}$ , red squares). The activation energy map model (solid lines) in Fig. 10 shows a very good agreement with all three measurements and demonstrates the good accuracy of this approach. For the first time, the fWLR data and the standard qualification measurement data are comparable using the activation energy maps. This enables that fWLR drift limits for the fabrication can be obtained from standard qualification measurements.

The second application is for the modeling of burn-in stress. A burn-in test is a test to screen weak components that would fail during the qualified lifetime. Therefore, the components are stressed under high bias up to 48 h. The threshold voltage shift under such a burn-in test is shown in Fig. 11 for three different burn-in stress conditions. For all three tests, the stress time is 100 ks,  $T_{\text{stress}} = 150^\circ\text{C}$ , and  $V_{\text{gs}} = -2.2 \text{ V}$ . Since in standard burn-in tests, the stressed devices are taken out of the oven after 1 h recovery at  $T = 150^\circ\text{C}$  and cooled down to  $T = 30^\circ\text{C}$ , we compare the recovery of the threshold voltage shift after dc stress for two recovery conditions:



**Fig. 11.** Measurements and simulation of the recovery of the threshold voltage shift after burn-in stress with  $V_{gs} = -2.2$  V,  $T_{stress} = 150$  °C with the  $x$ -axis the equivalent recovery time  $\Theta(30$  °C). Blue: stress voltage applied during cool-down, recovery at  $T_{rec} = 30$  °C.  $\Theta(30$  °C) corresponds to the actual measurement time. Red:  $T_{stress} = T_{rec} = 150$  °C. Orange: recovery of the threshold voltage shift after 100 ks square wave ac stress at  $T_{stress} = 150$  °C with  $V_{gs, low} = -2.2$  V and  $V_{gs, high} = 0$  V with a duty cycle of 0.5 and a frequency of 100 kHz. The solid (sum of permanent and recoverable component) and dashed (only permanent component) lines are simulated using the activation energy map.

1)  $T_{rec} = 30$  °C with applied stress voltage during cool-down (blue dots) and 2) with the recovery at  $T_{rec} = 150$  °C (red dots). After 1-h recovery at  $T_{rec} = 150$  °, the sample is cooled down to  $T_{rec} = 30$  °C, but since more than  $10^8$  s of equivalent recovery time  $\Theta(30$  °C) already passed, no further recovery is observed within the next 24 h. The solid (sum of permanent and recoverable component) and dashed (only permanent component) lines are simulated using the activation energy map. The measurement delay at  $T_{rec} = 150$  °C is the same as for  $T_{rec} = 30$  °C, but since the recovery temperature is higher, the recovery is accelerated and the shortest measurable equivalent recovery time  $\Theta(30$  °C) increases from  $t_d = 1$   $\mu$ s to  $t_d = 20$  ms.

The comparison of the dc measurements at  $T_{rec} = 30$  °C and  $T_{rec} = 150$  °C shows that with the lower recovery temperature up to four decades of measurement time are gained. Furthermore, the recovery of the threshold voltage shift after ac stress at  $T_{rec} = 150$  °C is shown (orange dots). The degradation after a 100-ks ac burn-in stress  $T_{stress} = 150$  °C with a 100-kHz square wave signal with  $V_{gs, low} = -2.2$  V and  $V_{gs, high} = 0$  V, and a duty cycle of 0.5 is significantly lower compared to the dc stress. The permanent component dominates the threshold voltage shift, and thus, even at a recovery temperature of  $T_{rec} = 150$  °C only a small portion of recovery can be observed. All simulations show a very good agreement with the three measurements and can be used to compare burn-in measurements during fabrication with lifetime models obtained during qualification.

## VI. INVESTIGATING THE PERMANENT COMPONENT OF NBTI

$\Delta V_{th}$  after NBTI stress typically decreases monotonically with recovery time. Under special stress and recovery conditions, irregularities during the recovery have been observed [23]. This so-called reverse recovery behavior appears at high-stress temperatures ( $T > 200$  °C), long stress times, and after long recovery times ( $t_s \approx t_r \approx 100$  ks). The TA-MSM technique has been used to accelerate and study this phenomenon. In Fig. 12, the degradation after different

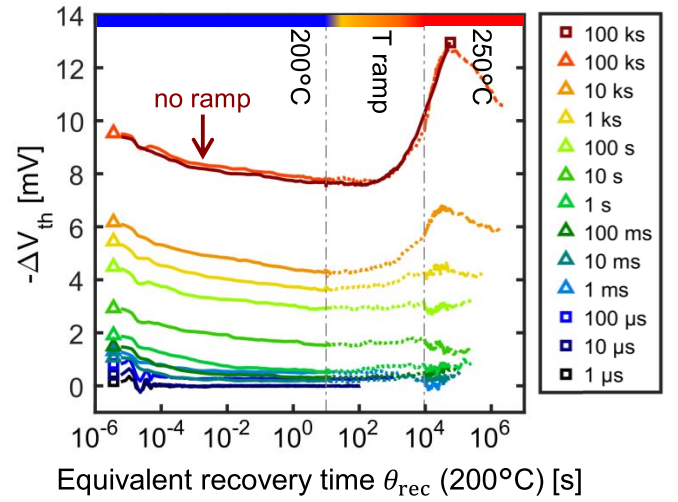


**Fig. 12.** Accelerated MSM measurement with  $V_{gs} = -1$  V,  $T_{ref} = 200$  °C. Each measurement after stress starts with recovery at  $T = 200$  °C of 100 s, followed by a linear temperature ramp within 500 s from 200 °C to 250 °C and further recovery of up to 50 ks at 250 °C. Squares and triangles: measurement scheme shown in Fig. 2(a) and (b). Red dark curve: degradation after 100 ks without temperature acceleration and  $T_{stress} = T_{rec} = 200$  °C.

stress times with  $T_{stress} = 200$  °C and  $V_{gs} = -1$  V is shown. After 100-s recovery at  $T_{rec} = 200$  °C, the temperature is linearly increased from 200 °C to 250 °C within 500 s. The  $x$ -axis is the temperature-time  $\Theta(200$  °C) calculated with the previously obtained  $\tau_{0, p}$  of 0.57 ns. For the  $> 10$ -ks stress measurements, the recovery starts to turn around, as poststress degradation builds up. This reverse recovery effect increases with increasing stress time. We compare the degradation after 100 ks without temperature acceleration and  $T_{stress} = T_{rec} = 200$  °C (dark red) with the accelerated reverse recovery during the temperature ramp (light red). The recovery measurement at constant temperature and the recovery measurement with the temperature ramps are fully equivalent for  $\Theta(200$  °C) calculated with  $\tau_{0, p}$ . This indicates that the more permanent defects are involved in this process. To conclude, instead of waiting months to fully observe the reverse recovery effect, temperature acceleration can also be used to accelerate this phenomenon which therefore makes it an invaluable tool to further investigate the permanent component of NBTI. Most importantly, while interesting from a physical perspective, we recall that this phenomenon is not observed at normally used stress temperatures below  $T = 200$  °C and is not observed in our accelerated MSM measurements, and therefore, also not included in our activation energy maps. This effect does not influence our lifetime calculations, because the effect occurs after the end of life of, e.g., 10 years for typical industrial use temperatures below  $T = 150$  °C [23].

## VII. CONCLUSION

For the first time, temperature acceleration of NBTI for both stress and recovery has been considered together leading to a unified activation energy map. We demonstrate a new temperature acceleration technique which can significantly reduce measurement time effort by, e.g., a factor of 10 ( $T = 100$  °C–200 °C). For the TA-MSM technique, no polyheater structures are needed and the number of samples compared to



MSM measurements at constant temperatures can be reduced. This measurement technique enables lifetime calculation of NBTI without gate voltage acceleration and time extrapolation solely with temperature acceleration. In addition, it is possible to perform measurements within an acceptable effort to obtain the full gate and recovery voltage dependence over the whole transistor lifetime for the use in circuit simulators. We show the application of the activation energy map model for the simulation of standard qualification measurements, fWLR resistive heater measurements, and burn-in stress tests. Before this investigation, a comparison of fWLR, burn-in tests, and qualification measurement was nearly impossible due to different temperatures, measurement times, and measurement schemes. Furthermore, the presented acceleration technique enables the study of the permanent component of NBTI and the recently discovered reverse recovery effect with acceptable measurement time effort.

## REFERENCES

- [1] J. P. Campbell, P. M. Lenahan, C. J. Cochrane, A. T. Krishnan, and S. Krishnan, "Atomic-scale defects involved in the negative-bias temperature instability," *IEEE Trans. Device Mater. Rel.*, vol. 7, no. 4, pp. 540–557, Dec. 2007, doi: [10.1109/TDMR.2007.911379](#).
- [2] M. Denais *et al.*, "Interface trap generation and hole trapping under NBTI and PBTI in advanced CMOS technology with a 2-nm gate oxide," *IEEE Trans. Device Mater. Rel.*, vol. 4, no. 4, pp. 715–722, Dec. 2004, doi: [10.1109/TDMR.2004.840856](#).
- [3] D. K. Schroder and J. A. Babcock, "Negative bias temperature instability: Road to cross in deep submicron silicon semiconductor manufacturing," *J. Appl. Phys.*, vol. 94, no. 1, pp. 1–18, Jun. 2003, doi: [10.1063/1.1567461](#).
- [4] J. H. Stathis, "The physics of NBTI: What do we really know?" in *Proc. Int. Rel. Phys. Symp. (IRPS)*, Burlingame, CA, USA, Mar. 2018, pp. 2A.1-1–2A.1-4, doi: [10.1109/IRPS.2018.8353539](#).
- [5] B. Kaczer *et al.*, "A brief overview of gate oxide defect properties and their relation to MOSFET instabilities and device and circuit time-dependent variability," *Microelectron. Rel.*, vol. 81, pp. 186–194, Feb. 2018, doi: [10.1016/j.microrel.2017.11.022](#).
- [6] T. Grasser, "Stochastic charge trapping in oxides: From random telegraph noise to bias temperature instabilities," *Microelectron. Rel.*, vol. 52, no. 1, pp. 39–70, Jan. 2012, doi: [10.1016/j.microrel.2011.09.002](#).
- [7] B. Kaczer *et al.*, "NBTI from the perspective of defect states with widely distributed time scales," in *Proc. Int. Rel. Phys. Symp. (IRPS)*, Montreal, QC, Canada, Apr. 2009, pp. 55–60, doi: [10.1109/IRPS.2009.5173224](#).
- [8] J. H. Stathis, S. Mahapatra, and T. Grasser, "Controversial issues in negative bias temperature instability," *Microelectron. Rel.*, vol. 81, pp. 244–251, Feb. 2018, doi: [10.1016/j.microrel.2017.12.035](#).
- [9] V. Huard, M. Denais, and C. Parthasarathy, "NBTI degradation: From physical mechanisms to modelling," *Microelectron. Rel.*, vol. 46, no. 1, pp. 1–23, Jan. 2006, doi: [10.1016/j.microrel.2005.02.001](#).
- [10] V. Huard, "Two independent components modeling for negative bias temperature instability," in *Proc. Int. Rel. Phys. Symp. (IRPS)*, Anaheim, CA, USA, May 2010, pp. 2A.4–2A.4.10, doi: [10.1109/IRPS.2010.5488857](#).
- [11] H. Reisinger, O. Blank, W. Heinrigs, A. Muhlhoff, W. Gustin, and C. Schlünder, "Analysis of NBTI degradation- and recovery-behavior based on ultra fast VT-measurements," in *Proc. Int. Rel. Phys. Symp. (IRPS)*, San Jose, CA, USA, Mar. 2006, pp. 448–453, doi: [10.1109/RELPHY.2006.251260](#).
- [12] K. Puschkarsky, H. Reisinger, C. Schlünder, W. Gustin, and T. Grasser, "Fast acquisition of activation energy maps using temperature ramps for lifetime modeling of BTI," in *Proc. Eur. Solid-State Device Res. Conf. (ESSDERC)*, unpublished, Sep. 2018.
- [13] T. Grasser, H. Reisinger, P.-J. Wagner, F. Schanovsky, W. Goes, and B. Kaczer, "The time dependent defect spectroscopy (TDDS) for the characterization of the bias temperature instability," in *Proc. Int. Rel. Phys. Symp. (IRPS)*, Anaheim, CA, USA, May 2010, pp. 16–25, doi: [10.1109/IRPS.2010.5488859](#).
- [14] G. Pobegen and T. Grasser, "On the distribution of NBTI time constants on a long, temperature-accelerated time scale," *IEEE Trans. Electron Devices*, vol. 60, no. 7, pp. 2155–2248, Jun. 2013, doi: [10.1109/TED.2013.2264816](#).
- [15] G. Pobegen, T. Aichinger, M. Nelhiebel, and T. Grasser, "Understanding temperature acceleration for NBTI," in *IEDM Tech. Dig.*, Washington, DC, USA, Dec. 2011, pp. 27.3.1–27.3.4, doi: [10.1109/IEDM.2011.6131623](#).
- [16] T. Grasser *et al.*, "Analytic modeling of the bias temperature instability using capture/emission time maps," in *IEDM Tech. Dig.*, Washington, DC, USA, Dec. 2011, pp. 27.4.1–27.4.4, doi: [10.1109/IEDM.2011.6131624](#).
- [17] Y. Illarionov *et al.*, "Hot-carrier degradation and bias-temperature instability in single-layer graphene field-effect transistors: Similarities and differences," *IEEE Trans. Electron Devices*, vol. 62, no. 11, pp. 3876–3881, Nov. 2015, doi: [10.1109/TED.2015.2480704](#).
- [18] G. Rzepa *et al.*, "Complete extraction of defect bands responsible for instabilities in n and pFinFETs," in *Proc. IEEE Symp. VLSI Technol.*, Honolulu, HI, USA, Jun. 2016, pp. 1–2, doi: [10.1109/VLSIT.2016.7573437](#).
- [19] H. Reisinger, T. Grasser, K. Ermisch, H. Nielen, W. Gustin, and C. Schlünder, "Understanding and modeling AC BTI," in *Proc. Int. Rel. Phys. Symp. (IRPS)*, Monterey, QC, Canada, Apr. 2011, pp. 6A1.1–6A1.8, doi: [10.1109/IRPS.2011.5784542](#).
- [20] T. Aichinger, M. Nelhiebel, S. Einspieler, and T. Grasser, "In situ poly heater—A reliable tool for performing fast and defined temperature switches on chip," *IEEE Trans. Device Mater. Rel.*, vol. 10, no. 1, pp. 3–8, Mar. 2010, doi: [10.1109/TDMR.2009.2033467](#).
- [21] G. Pobegen, M. Nelhiebel, S. de Filippis, and T. Grasser, "Accurate high temperature measurements using local polysilicon heater structures," *IEEE Trans. Device Mater. Rel.*, vol. 14, no. 1, pp. 169–176, Mar. 2014, doi: [10.1109/TDMR.2013.2265015](#).
- [22] T. Grasser, B. Kaczer, H. Reisinger, P.-J. Wagner, and M. Toledano-Luque, "On the frequency dependence of the bias temperature instability," in *Proc. Int. Rel. Phys. Symp. (IRPS)*, Anaheim, CA, USA, Apr. 2012, pp. XT.8.1–XT.8.7, doi: [10.1109/IRPS.2012.6241938](#).
- [23] T. Grasser *et al.*, "Implications of gate-sided hydrogen release for post-stress degradation build-up after BTI stress," in *Proc. Int. Rel. Phys. Symp. (IRPS)*, Monterey, QC, Canada, Apr. 2017, pp. 6A-2.1–6A-2.6, doi: [10.1109/IRPS.2017.7936334](#).



**Katja Puschkarsky** (M'18) received the B.Sc. degree in physics from the Friedrich-Schiller-Universität Jena, Jena, Germany, in 2012, and the M.Sc. degree in physics from Ludwig-Maximilians-Universität München, Munich, Germany, in 2014. She is currently pursuing the Ph.D. degree with the Infineon Central Reliability Department, Munich, and, in close cooperation with, the Institute for Microelectronics, Technische Universität Wien, Wien, Austria.



**Hans Reisinger** received the Diploma degree in physics and the Ph.D. degree from the Technical University of Munich, Munich, Germany, in 1979 and 1982, respectively.

In 1986, he joined the Semiconductor Department, Infineon Technologies AG, Neubiberg, Germany. He is currently with the Infineon Central Reliability Department, Infineon Technologies AG, where he was involved in threshold instabilities of logic- and power-MOSFETs.



**Christian Schlünder** received the Dipl.-Ing. degree in electrical engineering and the Ph.D. degree from the Technische Universität Dortmund, Dortmund, Germany, in 1999 and 2006, respectively.

He joined Infineon Technologies AG, Neubiberg, Germany, as a member of the Corporate Research Department, later he changed over to the Reliability Group. He is currently a Senior Staff Engineer, where he manages qualifications of embedded memories of in-house and foundry technologies.



**Wolfgang Gustin** received the Diploma degree in physics from the University of Stuttgart, Stuttgart, Germany, in 1990, and the Ph.D. from the Max-Planck-Institut Stuttgart, Stuttgart, in 1994.

In 1998, he joined the DRAM Development Group, Infineon Technologies AG, Neubiberg, Germany. He is currently the Manager of the Device Reliability Group, Infineon Technologies AG, where he was involved in the design for reliability and radiation-induced reliability.



**Tibor Grasser** (SM'05–F'16) is currently the Head of the Institute for Microelectronics, Technische Universität Wien, Wien, Austria.

Mr. Grasser was a recipient of the Best and Outstanding Paper Awards at IRPS in 2008, 2010, 2012, and 2014, respectively, IPFA in 2013 and 2014, respectively, ESREF in 2008, and the IEEE EDS Paul Rappaport Award in 2011.